Evolution of Star Formation in the UKIDSS Ultra Deep Survey Field - II. Star Formation as a Function of Stellar Mass Between z = 1.46 and z = 0.63

Alyssa B. Drake[1,2], Chris Simpson[1], Ivan K. Baldry[1], Phil A. James[1], Chris A. Collins[1], Masami Ouchi[3], Suraphong Yuma[4,3], James S. Dunlop[5], Daniel J. B. Smith[6]

[1]*Astrophysics Research Institute, Liverpool John Moores University, IC2, Liverpool Science Park, 146 Brownlow Hill, Liverpool L3 5RF, UK*
[2]*CRAL, Observatoire de Lyon, Université Lyon 1, 9 avenue Charles André, 69561 Saint Genis Laval Cedex, France*
[3]*Institute for Cosmic Ray Research, The University of Tokyo, Kashiwa 277 8582, Japan*
[4]*Department of Physics, Faculty of Science, Mahidol University, Bangkok 10400, Thailand*
[5]*SUPA, Institute for Astronomy, University of Edinburgh, Royal Observatory, Edinburgh, EH9 3HJ, UK*
[6]*Centre for Astrophysics, Science and Technology Research Institute, University of Hertfordshire, Hatfield, Herts, AL10 9AB, UK*

24 September 2015

ABSTRACT

We present new results on the evolution of the cosmic star formation rate as a function of stellar mass in the SXDS-UDS field. We make use of narrow-band selected emission line galaxies in four redshift slices between $z = 1.46$ and $z = 0.63$, and compute stellar masses by fitting a series of templates to recreate each galaxy's star formation history. We determine mass-binned luminosity functions in each redshift slice, and derive the star formation rate density (ρ_{SFR}) as a function of mass using the [O III] or [O II] emission lines. We calculate dust extinction and metallicity as a function of stellar mass, and investigate the effect of these corrections on the shape of the overall $\rho_{SFR}(M)$. We find that both these corrections are crucial for determining the shape of the $\rho_{SFR}(M)$, and its evolution with redshift. The fully corrected $\rho_{SFR}(M)$ is a relatively flat distribution, with the normalisation moving towards lower values of ρ_{SFR} with increasing cosmic time/decreasing redshift, and requiring star formation to be truncated across all masses studied here. The peak of $\rho_{SFR}(M)$ is found in the $10^{10.5} < M_\odot < 10^{11.0}$ mass bin at $z = 1.46$. In the lower redshift slices the location of the peak is less certain, however low mass galaxies in the range $10^{7.0} < M_\odot < 10^{8.0}$ play an important part in the overall $\rho_{SFR}(M)$ out to at least $z \sim 1.2$.

Key words: cosmology:observations - surveys - galaxies:evolution - galaxies:formation - galaxies:high-redshift - galaxies:luminosity functions.

1 INTRODUCTION

The evolution of cosmic star formation is well-studied, and crucial to our understanding of the Universe as a whole. It is now well-established that the peak of star formation activity lies beyond $z \sim 1$ (e.g. Hopkins & Beacom 2006) and that there has been a steep decline in this activity to the present day (Lilly et al. 1996, Le Floc'h et al. 2005, Prescott et al. 2009, Sobral et al. 2013, Drake et al. 2013). Determining the cosmic star formation rate density as a function of stellar mass however, $\rho_{SFR}(M)$, is somewhat more difficult, and the specifics of this aspect of observational cosmology are still obscure. Reports of a shift in the masses of star-forming galaxies across redshift are now commonplace, however the meaning of this is complex. Stars in massive galaxies are known to have formed earlier and on a shorter timescale than those formed in lower mass systems (Stanford et al. 1998, Heavens et al. 2004, Panter et al. 2007), and while this switch-off of star formation in massive galax-

ies is readily observed (e.g. Brodwin et al. 2013) and attributed to the feedback of an active galactic nucleus (AGN) truncating star formation, the behaviour of the lower mass star-forming population is less clear. For instance, the shift of the primary location of star formation activity from higher to lower mass galaxies with increasing time is clearly seen when considering specific star formation rates (sSFRs; star formation rates per unit stellar mass e.g. Noeske et al. 2007), however, this places only a weak constraint on the masses of objects dominating the overall ρ_{SFR} at each z.

In addition to AGN feedback in high mass galaxies, supernovae are known to expel gas from lower mass systems preventing the continuation of star formation (Oppenheimer & Davé 2008), and recent work has suggested that ~ 3 percent of star forming galaxies at $z \sim 1$ may have their star formation truncated through outflows of gas (e.g. Yuma et al. 2013). Determining the role of low-mass galaxies and establishing the true shape of the overall $\rho_{SFR}(M)$ is therefore the first step towards uncovering the relative

importance of the physical processes at work in truncating star formation.

The Redshift One LDSS3 Emission Line Survey (ROLES; Davies et al. 2009) was established to address the role of low-mass galaxies in the overall ρ_{SFR} as a function of mass and selected a sample of dwarf galaxies $10^{8.5} < M_{\odot} < 10^{9.5}$ at $z \sim 1$. Gilbank et al. (2010) used [O II] emission to estimate star formation rates (SFRs) for these galaxies and concluded that the shape of $\rho_{SFR}(M)$ does not evolve with redshift between $z \sim 1$ and the present day, a result since corroborated by Peng et al. (2010) and Sobral et al. (2014) who have both reported little change in the mass function of star-forming galaxies since $z \sim 1$.

The strong [O II] emission line doublet (3726Å and 3729Å) used in Gilbank et al. (2010) provides a particularly useful tool to trace star formation at redshifts >1 where Hα is shifted out of the optical window, and yet constraints on SFR via [O II] emission are estimated with a number of caveats. The traditional conversion between observed L[O II] and SFR (Kennicutt 1998) determines the average [O II]/Hα ratio for a sample of 90 local star-forming galaxies, and uses this to convert the apparent [O II] luminosity to an Hα-derived estimate of the SFR. Applying this relation to different samples of galaxies however, particularly if these are split by stellar mass, renders the relationship invalid as the average reddening from Hα to [O II] of samples at different masses may be drastically different to local star-forming galaxies.

Extinction is a frequently occurring obstacle for extragalactic astronomy, and many studies have attempted to quantify the effects and dependence of extinction on other physical parameters, e.g. stellar mass, metallicity or SFR (Heckman et al. 1998, Hopkins et al. 2001, Brinchmann et al. 2004, Asari et al. 2007, Garn et al. 2010a). Using the Balmer decrement, Garn & Best (2010) found that for a star-forming galaxy, extinction correlates most strongly with stellar mass, and propose a new relationship to describe this relationship calibrated for Hα luminosity but which can be extrapolated to other wavelengths.

As an additional consideration when using a metal line to determine SFR, one must account for the effect of the gas-phase metallicity on the strength of the lines. The [O III] and [O II] forbidden lines for instance are sensitive to metal abundances in addition to the temperature of the gas (Jansen et al. 2001, Charlot et al. 2002). In previous work Gilbank et al. (2010) for example applied an empirical correction to simultaneously account for the effects of both extinction and metallicity on the [O II] indicator. As an alternative however, Kewley, Geller & Jansen (2004) determine a conversion between intrinsic L[O II] and SFR which is thus independent of the reddening between the wavelengths of Hα and [O II], and also includes an optional correction for the metallicity of the gas. This relationship can then be applied to the intrinsic [O II] luminosities (i.e. those corrected for extinction at the wavelength of [O II]) of any sample of galaxies.

Understanding the evolution of $\rho_{SFR}(M)$ requires a dataset with a number of attributes. In addition to the requirement of a reliable SFR indicator, the data must be deep to probe low SFR objects, as well as sampling a wide range of masses. This problem is well suited to a narrow-band-selected sample where objects are detected via line emission across a wide range of masses and are close to SFR-limited (e.g. Sobral et al. (2014) who select star-forming galaxies based on their Hα emission to examine the evolution of the SFR and mass functions between $z = 2.23$ and $z = 0.40$).

In this paper, we utilise the ability of narrow-band selection to detect large numbers of star–forming galaxies irrespective of their stellar mass, to allow a statistical evaluation of the objects' prop-

erties as a function of mass. We build on the work of Drake et al. (2013) by determining stellar masses for objects in the four redshift slices covered by deep Subaru data at $z = 0.63$, $z = 0.83$, $z = 1.19$ and $z = 1.46$. We fit maximum likelihood luminosity functions to our sample using [O III] or [O II] emission in a series of mass bins to examine the resultant values of ρ_{SFR}. We incorporate a careful treatment of extinction and metallicity effects as a function of stellar mass, calibrating the dependence of SFR on metallicity down to $10^{7.0} < M_{\odot} < 10^{8.0}$. We aim to highlight the effect of these corrections on the shape of the $\rho_{SFR}(M)$ and consider the implications for the physical processes required to produce the fully corrected $\rho_{SFR}(M)$.

This paper proceeds as follows: in Section 2 we describe in brief the data used for this analysis, in Section 3 we explain the methods used to determine stellar masses, produce mass-binned luminosity functions, calculate star formation rates and the corrections applied to allow a treatment of extinction and metallicity as a function of stellar mass. In Section 4 we present our results in the form of luminosity functions and values of ρ_{SFR} per mass bin before discussing the factors affecting our results and the scientific implications of the shape of the fully corrected $\rho_{SFR}(M)$ between redshifts 1.46 and 0.63. We then draw conclusions in Section 6.

For consistency with the manner in which we calculate stellar masses all values of ρ_{SFR} are calculated for a Chabrier IMF. An $H_0 = 70$ kms^{-1} Mpc^{-1}, $\Omega_M = 0.3$ and $\Omega_\Lambda = 0.7$ cosmology is assumed throughout, and all magnitudes are in the AB system.

2 DATA AND SAMPLE SELECTION

We use data from the Subaru/XMM-Newton Deep Survey (SXDS; Furusawa et al. 2008) and the UKIDSS Ultra Deep Survey (UDS; Foucaud et al. 2007). The samples discussed in this paper are drawn from the catalogue of Drake et al. (2013), and are selected using two narrow-band filters on the Subaru Telescope at 8150 Å (NB816) and 9183 Å (NB921). The observations are complemented by 11 bands of photometry: CFHT u-band, Subaru B, V, R, i and z bands, UKIRT J, H and K bands, and *Spitzer* IRAC coverage in channels 1 and 2 (see table 1 of Drake et al. 2013 for further details). The narrow-band imaging has been smoothed using a Gaussian kernel, in order to match the point spread function (PSF) of the SXDS broad-band data (Ouchi et al. 2008, 2009).

Objects are selected according to their narrow-band excess, requiring a 5σ detection in the narrow band, a colour excess of at least 3σ above the sigma-clipped median intrinsic colour, *and* of at least 3σ relative to scatter introduced through photometric uncertainty.

The sample of line-emitters is cleaned of late-type stellar contaminants via the BzK technique of Daddi et al. (2004), and photometric redshifts are determined using the photometric redshift-fitting software "EAzY", making full use of the 11-band photometry to assign objects to redshift slices. This approach results in photometric redshifts with a normalised median absolute deviation of $\sigma_{NMAD} = 0.026$.

Finally, the completeness of detection in the narrow-band sample is assessed per $\Delta m_{NB} = 0.05$ bin using randomly positioned fake objects. The stringent 5σ detection limit means the effect is small, and only small numbers of objects need to be accounted for in the maximum likelihood analysis.

Full details can be found in Drake et al. (2013) of data coverage, sample selection, photometric redshift determination and assignment to redshift slices (via stacked probability density distri-

Table 1. Objects per redshift slice

Filter	Redshift slice	Emission Line	Objects
NB816	0.35 < **0.63** < 0.80	[O III]	999
NB921	0.50 < **0.83** < 1.10	[O III]	894
NB816	0.80 < **1.19** < 1.50	[O II]	956
NB921	1.10 < **1.46** < 1.90	[O II]	2203

butions) plus further information on the maximum likelihood approach to luminosity functions. Table 1 gives numbers of objects in each redshift slice used here.

3 METHOD

3.1 Stellar Masses

We determine stellar masses following the method of Simpson et al. (2012). Each object's redshift is set to the median redshift of the redshift slice, and the SED is fit with a series of synthetic star formation histories (SFHs) using the redshift–fitting sofware EA*z*Y to determine the most probable scenario for the galaxy's assembly. Simpson et al. (2012) design a set of 40 SFH templates based on instantaneous starbursts using a Chabrier IMF and the spectral models of Charlot and Bruzual (2007). The SFH templates range between very young populations, $\sim 20 \times 10^6$ years old, up to populations 13×10^9 years old. Finer time resolution is used between the younger templates, and a few young reddened templates are also included. The advantage of this approach is the ability to recreate *any* SFH through combination of instantaneous starburst templates. As this calculation is based on 2 arcsecond aperture fluxes from the catalogue described in Drake et al. (2013) however, each mass must be scaled by the ratio of total K-band flux to aperture K-band flux. Here we use total K flux values from the catalogue of Grützbauch et al. (2011) where available, or a 2.2 arcsecond aperture flux to simulate total K-band flux otherwise.

Figure 1 shows a comparison of masses derived in this work and the stellar mass estimates of the same objects detected in Hartley et al. (2013). Not all of the star-forming galaxies detected in our survey are found in the K-band selected sample of Hartley et al. (2013), however where the samples overlap our stellar masses agree well with the published work. Our use of the Charlot and Bruzual (2007) models which incorporate a greater contribution from thermally pulsing (TP-) AGB stars, results in lower masses by $0.1 - 0.2$ dex than those of the Bruzual & Charlot 2003 models used in Hartley et al. (2013).

3.2 Mass-Binned Maximum-Likelihood Luminosity Functions

Drake et al. (2013) described our method of determining maximum likelihood luminosity functions for narrow-band selected samples, and demonstrated that this approach possesses a number of advantages over existing techniques. We now apply this method to mass-binned data at $z = 0.63$, $z = 0.83$, $z = 1.19$ and $z = 1.46$ to determine luminosity functions as a function of stellar mass. A small but important difference between this analysis and that of Drake et al. (2013), is the manner in which we model the underlying star-forming galaxy population. For the original analysis the population of broad-band selected galaxies in a redshift slice was well fit by a Schechter function, however splitting the sample by stellar mass,
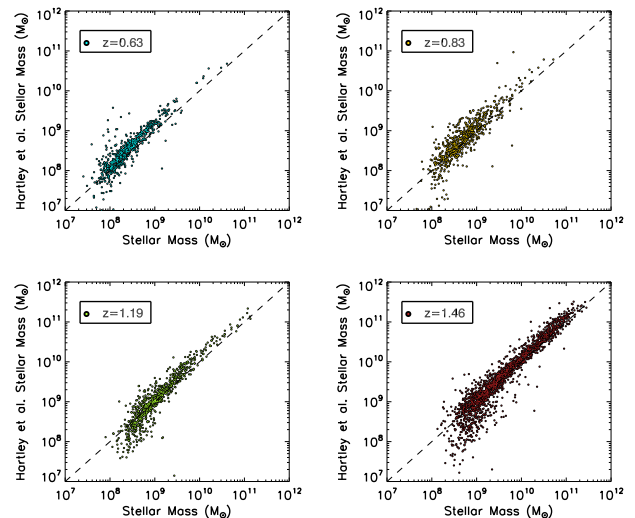
Figure 1. Comparison of stellar mass estimates from this work and results in the literature from Hartley et al. 2013. The four panels represent the 4 redshift slices we have used for this analysis progressing from top left to bottom right in increasing redshift order $z = 0.63, 0.83, 1.19, 1.46$.

this approach is obviously no longer appropriate. We find the best fit when this population is modelled as a Gaussian (see Figure 2), and so we use this to represent the broad-band magnitudes of galaxies in each mass range from the K-band selected catalogue of Simpson et al. (2012). For each redshift slice we fit to the observed broad band corresponding to the rest-frame wavelength of the NB selection filter, i.e. for NB816-selected objects this is an interpolation of the i and z bands, and for NB921-selected objects z-band only. The Simpson et al. (2012) catalogue is used here in preference to Grützbauch et al. (2011) or Hartley et al. (2013) for consistency in stellar mass estimates only.

Each redshift slice is split into $5 - 7$ mass bins (depending on the number of detections and range of stellar masses) of width 1 dex in the lowest mass bin ($10^{7.0} < M_\odot < 10^{8.0}$) and 0.5 dex for the remainder of the sample.

3.3 Star Formation Rates

To investigate the effects of different assumptions about dust and metallicity on the resultant SFRs, we compute ρ_{SFR} using a series of different approaches.

To determine SFR from $L_{[OIII]}$ we initially take the same approach as in Drake et al. (2013) and apply the standard line ratios: Hα/Hβ=2.78 and [O III]/Hβ=3 (Osterbrock & Ferland 2006) to convert the Kennicutt (1998) relation between $L_{H\alpha}$ and SFR to one for $L_{[OIII]}$ (Equation 1):

$$SFR(M_\odot yr^{-1}) = 7.35 \times 10^{-35} L_{[OIII]} E_{[OIII]} \qquad (1)$$

where $L_{[OIII]}$ is the observed [O III] luminosity, and $E_{[OIII]}$ represents extinction at the wavelength of [O III]. The Kennicutt (1998) approximation of SFR for $L_{[OII]}$ is computed according to Equation 2:

$$SFR(M_\odot yr^{-1}) = 1.39 \times 10^{-34} L_{[OII]} E_{H\alpha} \qquad (2)$$
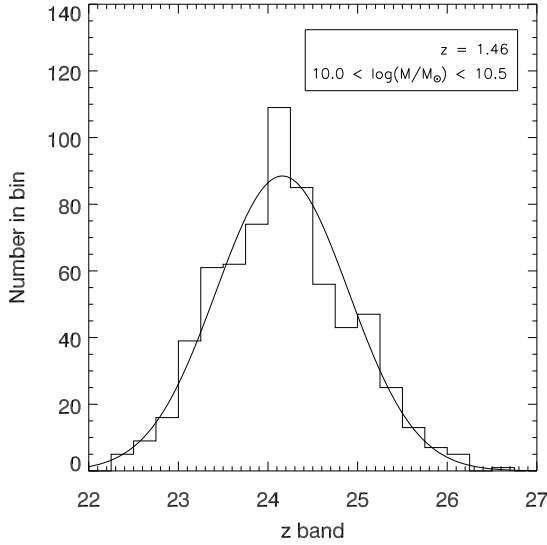
Figure 2. Example of Gaussian fit to the distribution of broad-band magnitudes at $z = 1.46$ in the $10.0 < \log(M/M_\odot) < 10.5$ mass bin. For these NB921-selected objects this is the z band magnitude, taken from the K-band selected catalogue of Simpson et al. (2012)

where $L_{[OII]}$ is the observed [O II] luminosity, and $E_{H\alpha}$ represents extinction at the wavelength of Hα.

3.3.1 Mass- Dependent Extinction Correction

Extinction is known to correlate with a number of physical properties of galaxies (Brinchmann et al. 2004, Garn et al. 2010b) the dominant of these being stellar mass (Garn & Best 2010). To address the mass-dependence of dust extinction, we implement Equation 3 of Garn & Best (2010) to describe Hα extinction in magnitudes as a function of stellar mass:

$$A_{H\alpha} = 0.91 + 0.77x + 0.11x^2 - 0.09x^3 \tag{3}$$

where $x = \log_{10}(M/10^{10}M_\odot)$. Using Equation 3 we determine values for $A_{H\alpha}$ per mass bin and apply the Cardelli et al. (1989) reddening law to the set of values found for this prescription to determine the corresponding values of $A_{[OIII]}$ and $A_{[OII]}$. Each fit is set to a constant below $10^{9.0}M_\odot$ where the estimate is unreliable.

For $L_{[OIII]}$ estimates of SFR we use Equation 1 in conjunction with an assessment of the dust extinction per mass bin from Equation 3. For $L_{[OII]}$ however, the estimate of SFR from Equation 2 is affected by uncertainties due to the wavelength dependence of reddening between the Hα and [OII] lines. While this is the standard approach for large statistical samples, it is unsuitable for this dataset, binned by stellar mass and spanning a wide range of redshifts. Kewley et al. (2004) re-calibrate the [OII] indicator to be reddening independent, allowing for the application of SFR([OII]) to a wide range of galaxy samples. This is presented in Equation 4:

$$SFR([OII])(M_\odot yr^{-1}) = (6.58 \pm 1.65) \times 10^{-35} L_{[OII]} E_{[OII]} \tag{4}$$

where $L_{[OII]}$ is observed [O II] luminosity, and $E_{[OII]}$ is the flux
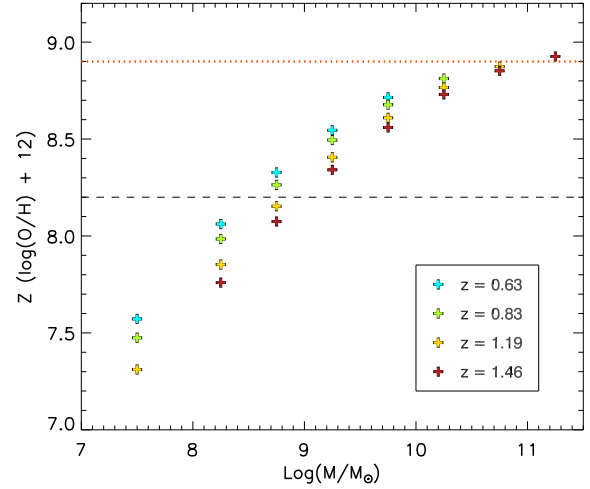
Figure 3. Metallicity per mass bin of width 0.5 dex. Metallicity is particularly low in the lower half of mass bins. Solar abundance in these units is 8.9 marked by the dark orange dotted line. The dashed horizontal line at 8.4 represents the limit of the metallicities modelled in the Kewley et al. (2004) calibration for SFR.

extinction at the wavelength of [O II]. We apply this conversion to determine ρ_{SFR} for galaxies with a dust extinction correction as a function of stellar mass, using Equation 3 in conjunction with the prescription of Cardelli et al. (1989) to determine $E_{[OII]}$.

3.3.2 Metallicity Correction

Although the [O III] and [O II] forbidden lines are sensitive to the the metallicity of a galaxy, Figure 11 of Kewley et al. (2004) shows that the ratio of [O III]/Hβ line luminosities is constant down to very low metallicities for a range of ionisation states of the gas, and hence we apply no metallicity correction for [O III]-derived estimates of SFR.

[O II] emission however varies considerably with gas-phase metallicity (here meaning oxygen abundance defined as $\log(O/H) + 12$), and since the traditional conversion of $L_{[OII]}$ to SFR relies on the relationship between observed [O II] to Hα, the variation with metallicity introduces an error in this approach. Kewley et al. (2004) build on their earlier work to incorporate the effect of metallicity on the [O II]/Hα ratio, and hence derive a theoretical calibration for SFR($L_{[OII]}$) as a function of $L_{[OII]}$ and metallicity. [1] :

$$SFR([OII], Z)_t (M_\odot yr^{-1}) = \frac{7.9 \times 10^{-35} L([OII])}{[OII]/H\alpha} \tag{5}$$

They use theoretical models to examine the dependence of the [O II]/Hα ratio on metallicity for a number of different ionisation states of the H II gas. The relationship for intrinsic [O II]/Hα line ratio on metallicity is then given by:

$$[OII]/H\alpha = a + bZ + cZ^2 + dZ^3 \tag{6}$$

where $Z = \log(O/H) + 12$, and and the coefficients a, b, c, and d originate from the best fit curve for metallicity abundance vs [O II]/Hα for the appropriate ionisation parameter.

For consistency with our assumption of [O III]/Hβ=3 in Drake et al. (2013), we adopt an ionisation parameter[2] $q = 4 \times 10^7$. This is equivalent to $\log U = -2.875$, where U, the commonly adopted ionisation parameter, is defined as $U = q/c$. Our choice is entirely consistent with recent detailed studies e.g. Nakajima & Ouchi (2014) who found $q = 1 \times 10^7 - 1 \times 10^8$, and also falls within the "normal" range of ionisation parameters found in Kewley et al. (2004), and Dopita et al. (2000): $q = 1 \times 10^7 - 8 \times 10^7$ cm s^{-1}. For $q = 4 \times 10^7$, $a = -1432.67$, $b = 470.545$, $c = -51.2139$ and $d = 1.84750$.

To derive metallicities for our sample we employ the empirical model of Savaglio et al. (2005) for the evolution of the mass-metallicity relation to high redshift. They derive an expression for the metallicity of a galaxy of a given stellar mass, at t_H, the age of the Universe at that redshift for the assumed cosmology, as:

$$12 + \log(\text{O/H}) = -7.5903 + 2.5315 \log M$$
$$-0.09649 \log^2 M + 5.1733 \log t_H - 0.3944 \log^2 t_H$$
$$-0.4030 \log t_H \log M.$$

(7)

We use Equation 7 to determine an average metallicity per mass bin, for each redshift slice. The resultant values can be seen in Figure 3, and reach substantially sub-solar values. The metallicity of the Sun is shown on this plot as the dotted orange line at Z=8.9.

For mass bins of very low metallicity (< 8.2, about half of our sample) the model fit to [O II]/Hα from Kewley et al. (2004) breaks down, and extrapolating the fit results in non-physical values of [O II]/Hα. The limit of the Kewley et al. (2004) model is shown as the dashed black line in Figure 3. Kewley et al. (2004) use PEGASE stellar population models (Fioc & Rocca-Volmerange 1997) with the STARBURST99 code (Leitherer et al. 1999) to determine an ionising spectrum to simulate values of [O II]/Hα, using the MAPPINGS III radiative transfer code (e.g. Sutherland & Dopita 1993) for different values of metallicity and ionisation parameter, q.

To determine values of [O II]/Hα we therefore follow the method of Kewley et al. (2004) but use the CLOUDY (Ferland et al. 2013) radiative transfer code to determine [O II]/Hα at each metallicity. We assume a total H density of $10^{2.5}$ cm^{-3} which corresponds to the electron density 350 cm^{-3} used in Kewley et al. (2004). The resultant values of [O II]/Hα agree to $\sim 10\%$ over the corresponding metallicity range.

The [O II]/Hα ratios are well fit in log space by Equation 8:

$$\log([\text{OII}]/\text{H}\alpha) = a + b\text{Z} + c\text{Z}^2 + d\text{Z}^3$$

(8)

with best fitting coefficients $a = 76.94$, $b = -33.86$, $c = 4.77$, and $d = -0.22$.

We use Equation 5 in conjunction with our own estimates of [O II]/Hα to determine fully corrected values of ρ_{SFR} based on [O II] luminosity.

---

[2] where q is the maximum velocity of the ionisation front driven by the local radiation field (Kewley et al. 2004)

4 RESULTS

4.1 Luminosity Functions

The mass-binned maximum-likelihood luminosity functions for objects at the weighted-mean redshift of emitters in a particular redshift slice are presented in Figure 4 and Table A1. Volumes quoted in the table are representative of the volume where narrow-band filter transmission is greater than 0.5. Values of L* are corrected for Galactic extinction and aperture effects. The data in Figure 4 are presented as in Drake et al. (2013), where the solid coloured line gives the maximum likelihood fit, and the data points on the plot are binned arbitrarily for presentation.

For each luminosity function the maximum likelihood analysis determines the most likely values of ϕ^*, L* and α, allowing all three parameters to vary. In order to produce a well-constrained fit however, the data must probe significantly below L* in the particular redshift/mass-bin combination. For some luminosity functions, the depth of the data coupled with a small number of emitters in that mass bin, result in poorly-constrained values of α. Where this is the case, we follow the approach taken in Drake et al. (2013), and constrain the luminosity function with a Gaussian prior on the faint end slope, set to the value of α for the closest mass bin in that redshift slice. A point of note is that in each case the sum of the mass-binned luminosity functions (denoted by the dashed line) including those with a Gaussian prior, is in good agreement with the best–fit luminosity function for the entire redshift slice (given by the solid black line). The small deviations between the two lines seen at the bright or faint end of the LFs can be explained by objects in the wings of the mass distributions where there were too few sources to fit a LF.

4.2 ρ_{SFR} as a Function of Stellar Mass

Figure 5 presents values of $\rho_{\text{SFR}}(M)$ evaluated considering an integration of the data to two different limits in the left and right hand panels, and incorporating various different approaches to the treatment of dust extinction and metallicity. The method used for each row of panels is detailed below and the corresponding values are summarised in Table B1. For consistency with the manner in which we calculate our stellar masses, the ρ_{SFR} values quoted and plotted have been converted to a Chabrier IMF.

Initially, ρ_{SFR} is computed using the Kennicutt (1998) relation and applying 1 magnitude of extinction at Hα (upper panels Figure 5). In the central panels of Figure 5, we determine extinction as a function of stellar mass according to the prescription of Garn & Best (2010) using Cardelli et al. (1989) to infer values at [O III] and [O II], and use Equation 4 of Kewley et al. (2004) to derive SFR([O II]). Finally, in the lower two panels we use our estimates of $\log(\text{O/H}) + 12$ to incorporate a metallicity correction in conjunction with Equation 5 of Kewley et al. (2004) to determine a fully corrected $\rho_{\text{SFR}}(M)$.

The appropriate limits of integration to determine ρ_{SFR} per mass bin are complicated for this analysis, since the sensitivity in M$_\odot$yr^{-1} varies considerably due to the use of two different emission line indicators and the range of redshift studied. Here we evaluate each luminosity function in two different ways; to the limit of the data in each redshift slice (left-hand panels Figure 5) and to the same limiting SFR in each redshift slice (right-hand panels Figure 5). In the former approach, the limiting SFRs are 0.08, 0.12, 0.55 and 1.42 M$_\odot$yr^{-1} at $z = 0.63, 0.83, 1.19$ and 1.46 respectively, producing sensible results for most mass bins. Intergrating to the same limiting SFR for comparison across redshift
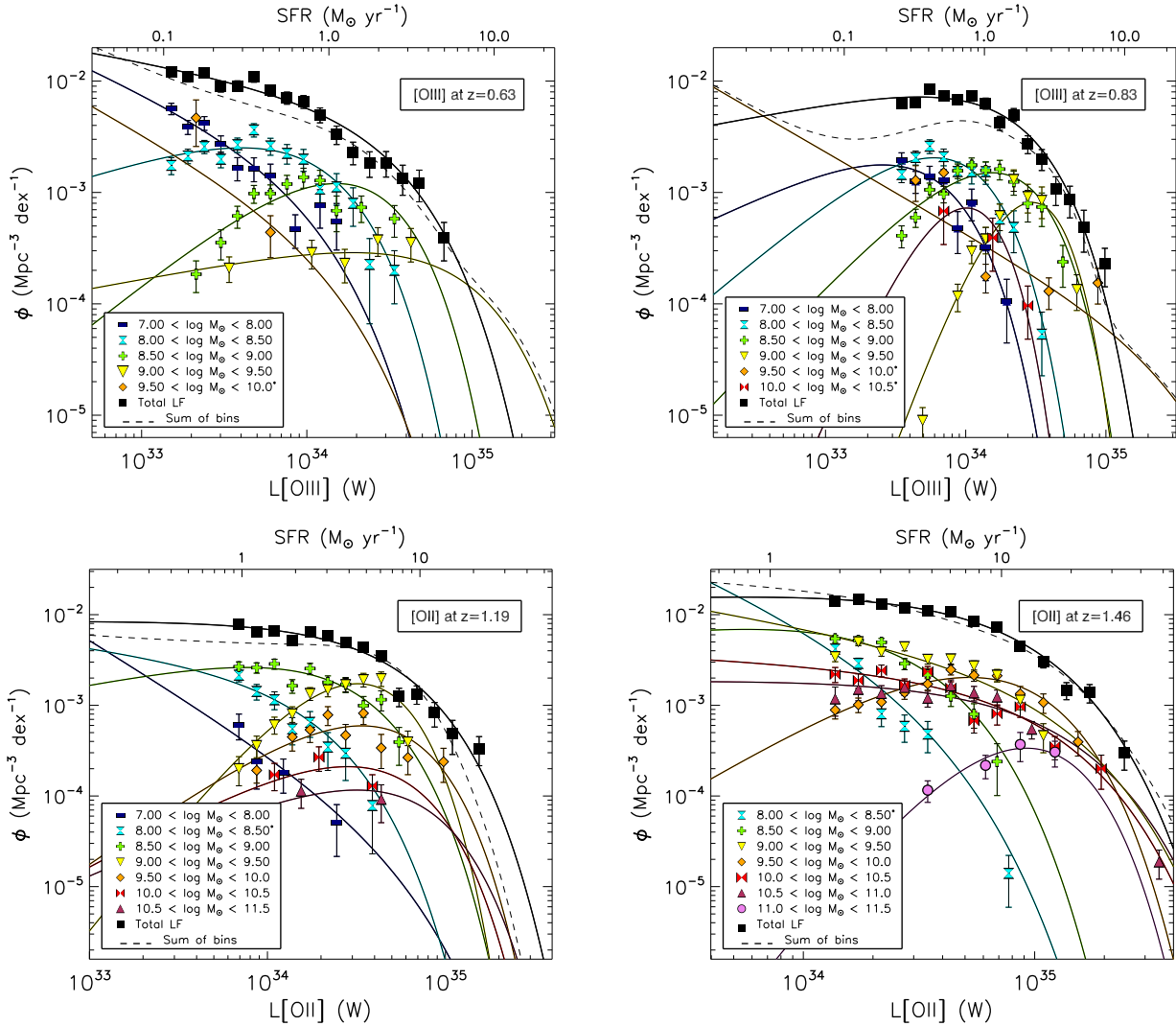
Figure 4. Best–fitting luminosity functions for redshift slices: $z = 0.63$ between 7.25 and 9.25 dex, $z = 0.83$ (7.75 to 10.25 dex), $z = 1.19$ (7.75 to 10.75 dex), $z = 1.46$ (7.75 to 11.25 dex). The upper SFR scale on these plots gives an indication of SFR values assuming a constant scaling from luminosity for these LFs. Neither these numbers nor the luminosities have been corrected for dust extinction.

slices however presents more of a challenge. Selections made in the $z = 0.63$ and $z = 0.83$ redshift slices can be integrated to low SFRs $\sim 0.1 M_\odot \text{yr}^{-1}$, however limits which produce sensible results for these redshift slices require a large extrapolation at $z = 1.19$ and $z = 1.46$ and consequently introduce a far greater uncertainty on luminosity functions that probe little below L*. Likewise, limiting the integration to values where the luminosity function is well-constrained in these redshift slices results in the loss of a large portion of the $\rho_{\text{SFR}}(M)$ in the lower redshift slices (additionally there is a dramatic drop in the $10^{9.5} < M_\odot < 10^{10.0}$ bin at $z = 0.63$ where the whole luminosity function is poorly constrained) and ultimately the best choice for a constant limiting SFR is $1 M_\odot \text{yr}^{-1}$. We include this analysis to provide a consistent evaluation across redshift, however we prefer values of $\rho_{\text{SFR}}(M)$ based on the limit of the data as being representative of the total SFR.

4.2.1   Errors on $\rho_{\text{SFR}}(M)$

Errors on ρ_{SFR} are first computed according to the maximum and minimum values that arise from the 1σ deviation of ϕ^*, L* and α when all three parameters are allowed to vary in the maximum-likelihood analysis. Additionally we quantify the uncertainty in ρ_{SFR} introduced through the small number of objects making up some mass bins by incorporating an additional Poissonian error. The initial 1σ error is combined with the fractional error on ρ_{SFR} according to Gehrels (1986) given the number of objects making up the luminosity function. Errors quoted in Table B1 and shown on Figure 5 represent the combination of these two errors in quadrature.
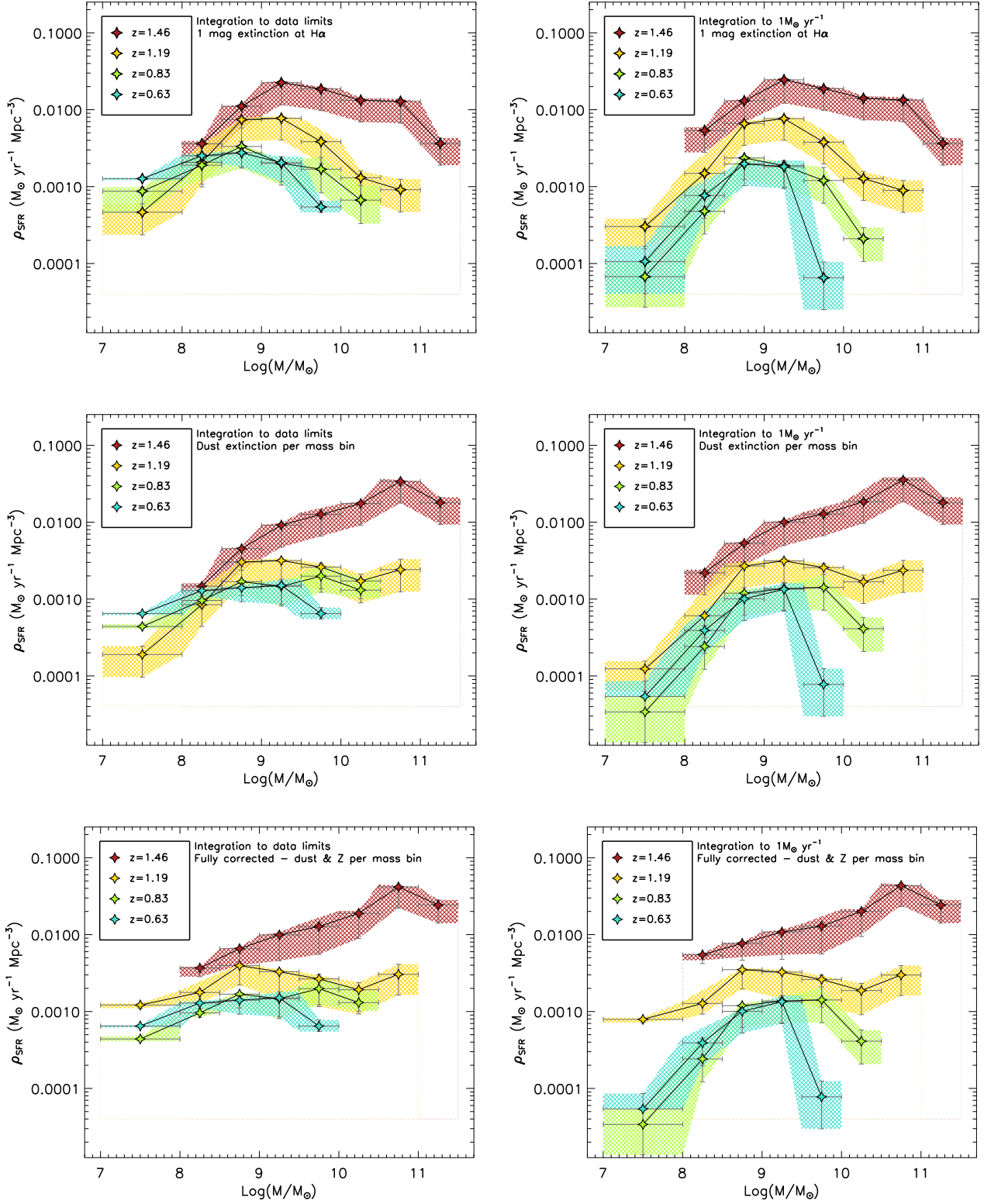
Figure 5. ρ_{SFR} as a function of mass for redshift slices at $z = 0.63$, $z = 0.83$, $z = 1.19$ and $z = 1.46$. ρ_{SFR} is estimated via Kennicutt (1998) and 1 mag extinction at Hα (top two panels), Kewley et al. (2004) and dust extinction as a function of stellar mass (central two panels), and the fully corrected ρ_{SFR} including dust an metallicity corrections (lower two panels). The left-hand column of figures present results for an integration to the limit of the data in each redshift slice, and the right hand column of figures presents an integration to $1 M_\odot \, yr^{-1}$.

5 DISCUSSION

5.1 The Effect of Dust and Metallicity Corrections on $\rho_{\mathrm{SFR}}(\mathrm{M})$

Applying 1 magnitude of extinction at Hα (top two panels of Figure 5) shows the peak of $\rho_{\mathrm{SFR}}(\mathrm{M})$ lying in the $10^{9.0}{<}\mathrm{M}_\odot{<}10^{9.5}$ bin at $z = 1.46$ and $z = 1.19$, shifting to $10^{8.5}{<}\mathrm{M}_\odot{<}10^{9.0}$ at $z = 0.83$, and $z = 0.63$, a feature which is preserved for both limits of integration. The most notable difference between the two approaches is the far lower values of $\rho_{\mathrm{SFR}}(\mathrm{M})$ in the two lower redshift slices due to the $1\mathrm{M}_\odot\mathrm{yr}^{-1}$ limit probing little below L*.

Incorporating dust corrections as a function of stellar mass (central two panels) produces a dramatic change in the shape of the $\rho_{\mathrm{SFR}}(\mathrm{M})$ for the redshift $z = 1.46$ slice, raising the high mass end ($>10^{10.0}\mathrm{M}_\odot$) significantly and lowering values of $\rho_{\mathrm{SFR}}(\mathrm{M})$ for all masses $<10^{10.0}\mathrm{M}_\odot$. Similarly the high-mass portions of $\rho_{\mathrm{SFR}}(\mathrm{M})$ in the $z = 1.19$ and $z = 0.83$ redshift slices are lifted, however in the $z = 0.63$ slice, little change is seen due to the lack of massive objects.

The lower two panels of Figure 5 present our best estimates of $\rho_{\mathrm{SFR}}(\mathrm{M})$ incorporating dust and metallicity corrections. Little change is seen across the central region of the function ($10^{8.0}{<}\mathrm{M}_\odot{<}10^{10.0}$) however a small rise is seen in masses $>10^{10.0}\mathrm{M}_\odot$, and a large increase below $10^{8.0}\mathrm{M}_\odot$. This low mass increase only affects the $z = 1.19$ slice since galaxies below $10^{8.0}\mathrm{M}_\odot$ do not enter the $z = 1.46$ selection, and the low mass objects at $z = 0.63$ and $z = 0.83$ have their SFRs computed via [O III] luminosity which requires no metallicity correction.

Figure 6 presents in a simple format the way each correction applied to the $\rho_{\mathrm{SFR}}(\mathrm{M})$ affects the shape of the function. In each panel the black shaded area and dashed line highlight the shape of the $\rho_{\mathrm{SFR}}(\mathrm{M})$ using the traditional assumptions about [O II]/Hα and the converison of Kennicutt (1998). The dashed orange line then gives the $\rho_{\mathrm{SFR}}(\mathrm{M})$ corrected only for dust extinction as a function of stellar mass, and the red dashed line gives the final $\rho_{\mathrm{SFR}}(\mathrm{M})$ corrected for extinction and metallicity (where appropriate) as a function of stellar mass for each redshift slice.

5.2 Evolution of $\rho_{\mathrm{SFR}}(\mathrm{M})$

We favour the lower left-hand panel of Figure 5 as representative of the fully-corrected $\rho_{\mathrm{SFR}}(\mathrm{M})$. The peak contribution to ρ_{SFR} at $z = 1.46$ comes from galaxies in the mass range $10^{10.5}{<}\mathrm{M}_\odot{<}10^{11.0}$, however in the lower redshift slices it is less clear where the peak of the function lies. The objects detected in the lower redshift slices do not reach masses as high as those at $z = 1.46$ and so it is impossible to say if the ρ_{SFR} is still rising at these masses. Figure 6 highlights how dust extinction as a function of mass kicks in at the highest masses which would act to raise the ρ_{SFR} considerably at the high masses which are missing from the lower two redshift slices.

The shape of the fully corrected $\rho_{\mathrm{SFR}}(\mathrm{M})$ is remarkably flat in comparison to the raw function, and shifts to lower normalisation with increasing time/decreasing redshift. A similar effect is seen in both Gilbank et al. (2010) and Sobral et al. (2014) who conclude that the shape of the ρ_{SFR} as a function of mass shows very little evolution with redshift. One thing we can note with this particular selection of galaxies is that galaxies of very low mass ($10^{7.0}{<}\mathrm{M}_\odot{<}10^{8.0}$) play an important part in the contribution to the overall ρ_{SFR} out to at least $z = 1.19$.
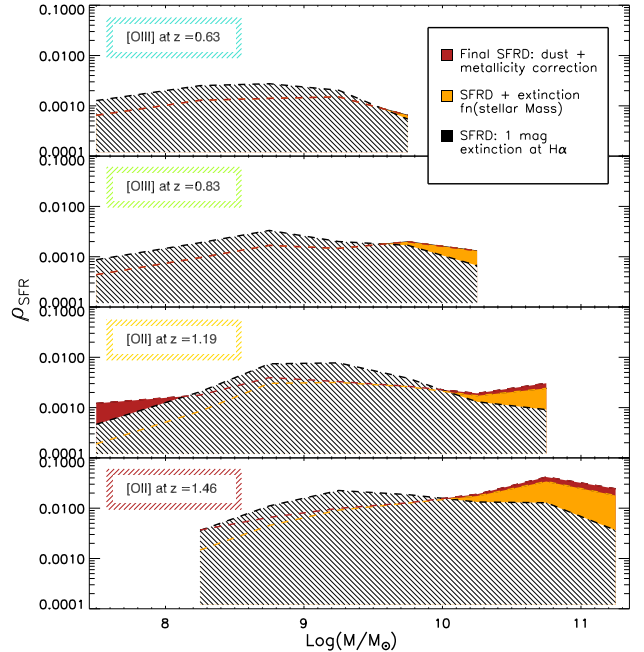

Figure 6. The shape of the ρ_{SFR} as estimated via Kennicutt (1998) and 1 mag extinction at Hα (black shaded region plus black dashed line), Kewley et al. (2004) and dust extinction as a function of stellar mass (orange shaded region and orange dashed line), and the fully corrected ρ_{SFR} including dust an metallicity corrections (red shaded region and red dashed line).

5.3 The Contribution of Different Masses to ρ_{SFR}

Considering galaxies in four mass bins where we have data points for all four redshift slices: $10^{8.0}{<}\mathrm{M}_\odot{<}10^{8.5}$ (cyan), $10^{8.5}{<}\mathrm{M}_\odot{<}10^{9.0}$ (green), $10^{9.0}{<}\mathrm{M}_\odot{<}10^{9.5}$ (yellow), $10^{9.5}{<}\mathrm{M}_\odot{<}10^{10.0}$ (orange), Figure 7 examines the contributions from galaxies of different masses to the overall ρ_{SFR}. The dotted line and green Σ symbols represent the sum of these four bins, and coloured points represent the contributions to ρ_{SFR} from each of these mass bins. Broadly speaking the relative contributions from the different mass bins decline simultaneously with the value of ρ_{SFR} itself. A notable feature however is the stronger decline in contribution from galaxies in the $10^{9.50}{<}\mathrm{M}_\odot{<}10^{10.0}$ bin relative to the lower mass bins. This is in contrast to the result of Sobral et al. (2014) where ρ_{SFR} of galaxies in all three mass bins presented in their figure 8 decline contemporaneously with the overall ρ_{SFR}. There are likely a number of reasons which lead to this discrepancy. Sobral et al. (2014) benefits from a consistently selected sample of Hα emitters across redshifts $z = 0.40$ - $z = 2.23$ meaning SFR is calculated homogeneously across the entire redshift range. In contrast we have estimated $\rho_{\mathrm{SFR}}(\mathrm{M})$ using [O III] ($z = 0.63, z = 0.83$) or [O II] ($z = 1.19, z = 1.46$) emission, indicators which are known to have a higher and less well understood contamination from AGN (see Section 5.4).

Additionally, slightly different (larger) mass bins are used for the Sobral et al. (2014) analysis, plus the larger range in redshift studied may allow the small fluctuations seen across the four redshift slices studied here to be smoothed out.
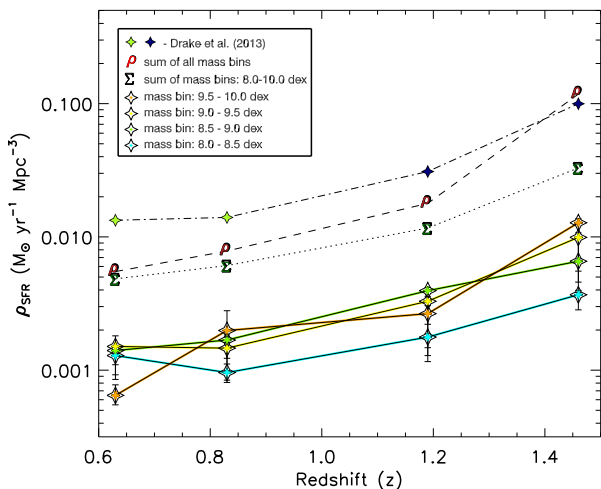
Figure 7. Contribution of galaxies of different masses to the overall ρ_{SFR} in the four redshift slices studied here. Dot-dashed lines and points thereon represent the overall ρ_{SFR} taken from Drake et al (2013) converted to a Chabrier IMF. The dashed line and rho symbols present the sum of all mass bins in this study, and the dotted line and capital Sigma symbols show the sum of the four mass bins examined here. $10^{8.0} < M_{\odot} < 10^{8.5}$ (cyan), $10^{8.5} < M_{\odot} < 10^{9.0}$ (green), $10^{9.0} < M_{\odot} < 10^{9.5}$ (yellow), $10^{9.5} < M_{\odot} < 10^{10.0}$ (orange)

5.4 The Effect of AGN Contamination on ρ_{SFR}

We can estimate the level of AGN-contamination by quantifying X-ray sources in the field that are coincident with the positions of our emission-line-selected sample. Using the catalogue of Ueda et al. (2008) and matching within a 3 arcsecond radius, we find small numbers of interlopers in each redshift slice: 7, 1, 0 and 9 objects are found in redshift slices $z = 0.63$, $z = 0.83$, $z = 1.19$ and $z = 1.46$ respectively, equating to 1 percent (to the nearest percentage point) in the lowest redshift slice, and less than this in all other bins.

We take the same approach as in Drake et al. (2013) and choose not to actively correct for AGN contamination, since those objects with AGN activity will undoubtedly be associated with some star formation, thus leading to a possible over correction.

We should however consider the consequences of possible AGN contamination. If, as many authors have suggested, AGN contamination rises towards higher redshift (e.g. 10 percent at $z < 1$, 15 percent at $z > 1$ Garn et al. 2010a, Sobral et al. 2013) the effect on ρ_{SFR} would be to lower estimates above $z = 1$ by a larger amount than estimates at $z < 1$, effectively moving the four coloured contours closer together, meaning there has been less evolution of the ρ_{SFR} than implied in Figure 5.

A second consideration is the likelihood of the higher mass bins being more highly contaminated by AGN than the lower mass bins. To place some constraint on whether this may be the case, we chose to compare the ratio of line flux with flux at restframe 2500 Å. While the measurements show a correlation, the highest mass objects show the largest discrepancy, with line fluxes that would produce a larger SFR than that from the restframe 2500 Å flux. This gives an indication that the highest mass bins could be overestimating ρ_{SFR} effectively boosting the peak of ρ_{SFR} at the high mass end. If this is the case then the shape of the $\rho_{SFR}(M)$ is infact flatter than depicted in Fig 5. The physical implications of this

scenario are that the decline of star formation activity is even less driven by the switch off of star formation in massive galaxies, and governed by a process (or processes) acting across the entire mass range.

6 CONCLUSIONS

We have applied the method described in Drake et al. (2013) to determine mass-binned luminosity functions in four redshift slices between $z = 1.46$ and $z = 0.63$. We have investigated the effect of extinction and metallicity corrections as a function of stellar mass, and examined the role of galaxies of different masses in their contribution to the overall ρ_{SFR}. Our main conclusions can be broadly summarised as follows:

- The correct use of dust and metallicity corrections as a function of stellar mass is essential to establishing the true shape of $\rho_{SFR}(M)$ and its evolution with redshift.

- The normalisation of the fully corrected $\rho_{SFR}(M)$ shifts to lower values with increasing cosmic time (decreasing redshift).

- The peak in $\rho_{SFR}(M)$ is seen in the $10^{10.5} < M_{\odot} < 10^{11.0}$ mass bin at $z = 1.46$. In the lower redshift slices the location of the peak is less certain.

- Low mass galaxies reaching $10^{7.0} < M_{\odot} < 10^{8.0}$ play an important part in the $\rho_{SFR}(M)$.

- The contribution to the overall ρ_{SFR} from galaxies across the $10^{8.0} < M_{\odot} < 10^{9.5}$ mass range is roughly constant between $z = 1.46$ and $z = 0.63$. The contribution from the $10^{9.5} < M_{\odot} < 10^{10.0}$ bin drops more noticeably.

In conclusion our results paint a picture in which the decline of cosmic star formation activity since $z \sim 1$ is the result of the decline in SFR across a broad range of masses, i.e. it can not be attributed simply to the switch-off of the most massive galaxies. This brings to the forefront the question of the physical processes required to execute such a decline, and the relative importance of the different quenching mechanisms at work in truncating star formation.

REFERENCES

Asari N. V., Cid Fernandes R., Stasińska G., Torres-Papaqui J. P., Mateus A., Sodré L., Schoenell W., Gomes J. M., 2007, MNRAS, 381, 263
Brinchmann J., Charlot S., White S. D. M., Tremonti C., Kauffmann G., Heckman T., Brinkmann J., 2004, MNRAS, 351, 1151
Brodwin M., et al., 2013, ApJ, 779, 138
Bruzual G., Charlot S., 2003, MNRAS, 344, 1000
Cardelli J. A., Clayton G. C., Mathis J. S., 1989, ApJ, 345, 245
Charlot S., Kauffmann G., Longhetti M., Tresse L., White S. D. M., Maddox S. J., Fall S. M., 2002, MNRAS, 330, 876

Daddi E., Cimatti A., Renzini A., Fontana A., Mignoli M., Pozzetti L., Tozzi P., Zamorani G., 2004, ApJ, 617, 746

Davies G. T., et al., 2009, MNRAS, 395, L76

Dopita M. A., Kewley L. J., Heisler C. A., Sutherland R. S., 2000, ApJ, 542, 224

Drake A. B., et al., 2013, MNRAS, 433, 796

Fioc M., Rocca-Volmerange B., 1997, A&A, 326, 950

Foucaud S., et al., 2007, MNRAS, 376, L20

Furusawa H., et al., 2008, ApJS, 176, 1

Garn T., Best P. N., 2010, MNRAS, 409, 421

Garn T., et al., 2010a, MNRAS, 402, 2017

Garn T., et al., 2010b, MNRAS, 402, 2017

Gehrels N., 1986, ApJ, 303, 336

Gilbank D. G., et al., 2010, MNRAS, 405, 2419

Grützbauch R., Chuter R. W., Conselice C. J., Bauer A. E., Bluck A. F. L., Buitrago F., Mortlock A., 2011, MNRAS, 412, 2361

Hartley W. G., et al., 2013, MNRAS, 431, 3045

Heavens A., Panter B., Jimenez R., Dunlop J., 2004, Nature, 428, 625

Heckman T. M., Robert C., Leitherer C., Garnett D. R., van der Rydt F., 1998, ApJ, 503, 646

Hopkins A. M., Beacom J. F., 2006, ApJ, 651, 142

Hopkins A. M., Connolly A. J., Haarsma D. B., Cram L. E., 2001, AJ, 122, 288

Jansen R. A., Franx M., Fabricant D., 2001, ApJ, 551, 825

Kennicutt Jr. R. C., 1998, ARA&A, 36, 189

Kewley L. J., Geller M. J., Jansen R. A., 2004, AJ, 127, 2002

Le Floc'h E., et al., 2005, ApJ, 632, 169

Leitherer C., et al., 1999, ApJS, 123, 3

Lilly S. J., Le Fevre O., Hammer F., Crampton D., 1996, ApJ, 460, L1

Nakajima K., Ouchi M., 2014, MNRAS, 442, 900

Noeske K. G., et al., 2007, ApJ, 660, L47

Oppenheimer B. D., Davé R., 2008, MNRAS, 387, 577

Osterbrock D. E., Ferland G. J., 2006, Astrophysics of gaseous nebulae and active galactic nuclei

Ouchi M., et al., 2008, ApJS, 176, 301

Panter B., Jimenez R., Heavens A. F., Charlot S., 2007, MNRAS, 378, 1550

Peng Y.-j., et al., 2010, ApJ, 721, 193

Prescott M., Baldry I. K., James P. A., 2009, MNRAS, 397, 90

Savaglio S., et al., 2005, ApJ, 635, 260

Simpson C., et al., 2012, MNRAS, 421, 3060

Sobral D., Smail I., Best P. N., Geach J. E., Matsuda Y., Stott J. P., Cirasuolo M., Kurk J., 2013, MNRAS, 428, 1128

Sobral D., Best P. N., Smail I., Mobasher B., Stott J., Nisbet D., 2014, MNRAS, 437, 3516

Stanford S. A., Eisenhardt P. R., Dickinson M., 1998, ApJ, 492, 461

Sutherland R. S., Dopita M. A., 1993, ApJS, 88, 253

Ueda Y., et al., 2008, ApJS, 179, 124

Yuma S., et al., 2013, ApJ, 779, 53

APPENDIX A: MAXIMUM LIKELIHOOD FITS

APPENDIX B: VALUES OF $\rho_{\mathrm{SFR}}(\mathbf{M})$

Table A1. Luminosity functions in mass bins for four redshift slices. Values presented here are raw results from maximum likelihood fitting. These numbers have not been corrected for aperture effects or dust extinction.

Log mass bin	Objects	$\log \phi^*_{[OIII]}$	$\log L^*_{[OIII]}$ (Watts)	$\alpha_{[OIII]}$
Redshift $z = 0.63$ Volume$= 8.09 \times 10^4$ Mpc^3				
$7.00 < \mathbf{7.50} < 8.00$	272	$-3.08^{+0.35}_{-0.55}$	$33.90^{+0.30}_{-0.21}$	$-1.66^{+0.40}_{-0.35}$
$8.00 < \mathbf{8.25} < 8.50$	380	$-2.60^{+0.08}_{-0.13}$	$33.86^{+0.14}_{-0.11}$	$-0.51^{+0.37}_{-0.33}$
$8.50 < \mathbf{8.75} < 9.00$	202	$-2.86^{+0.04}_{-0.07}$	$34.05^{+0.13}_{-0.12}$	$0.20^{+0.60}_{-0.46}$
$9.00 < \mathbf{9.25} < 9.50$	62	$-3.63^{+0.22}_{-0.37}$	$34.78^{+0.34}_{-0.27}$	$-0.72^{+0.63}_{-0.44}$
$9.50 < \mathbf{9.75} < 10.00$	12	$-13.52^{+\infty}_{-\infty}$	$37.86^{+\infty}_{-\infty}$	$-3.37^{+\infty}_{-\infty}$
$9.50 < \mathbf{9.75} < 10.00$ †	12	$-3.73^{+0.49}_{-0.90}$	$34.06^{+0.46}_{-0.26}$	$-1.81^{+0.56}_{-0.53}$
Redshift $z = 0.83$ Volume$= 12.35 \times 10^4$ Mpc^3				
$7.00 < \mathbf{7.50} < 8.00$	115	$-2.72^{+0.09}_{-0.28}$	$33.55^{+0.27}_{-0.19}$	$-0.39^{+1.12}_{-0.99}$
$8.00 < \mathbf{8.25} < 8.50$	250	$-2.62^{+0.05}_{-0.11}$	$33.68^{+0.15}_{-0.13}$	$0.07^{+0.71}_{-0.61}$
$8.50 < \mathbf{8.75} < 9.00$	315	$-2.77^{+0.04}_{-0.10}$	$34.00^{+0.12}_{-0.11}$	$0.33^{+0.60}_{-0.48}$
$9.00 < \mathbf{9.25} < 9.50$	122	$-3.97^{+0.55}_{-1.03}$	$33.84^{+0.17}_{-0.16}$	$2.73^{+1.67}_{-1.25}$
$9.50 < \mathbf{9.75} < 10.00$	47	$-5.34^{+\infty}_{-\infty}$	$35.78^{+\infty}_{-\infty}$	$-1.89^{+\infty}_{-\infty}$
$9.50 < \mathbf{9.75} < 10.00$ †	47	$-4.82^{+0.84}_{-1.46}$	$35.45^{+1.19}_{-0.59}$	$-1.73^{+0.50}_{-0.28}$
$10.00 < \mathbf{10.25} < 10.50$	12	$-3.68^{+\infty}_{-\infty}$	$34.24^{+\infty}_{-\infty}$	$-2.60^{+\infty}_{-\infty}$
$10.00 < \mathbf{10.25} < 10.50$ †	12	$-3.68^{+0.72}_{-0.95}$	$33.45^{+0.17}_{-0.13}$	$2.11^{+1.53}_{-1.54}$
Redshift $z = 1.19$ Volume$= 19.06 \times 10^4$ Mpc^3				
		$\log \phi^*_{[OII]}$	$\log L^*_{[OII]}$ (Watts)	$\alpha_{[OII]}$
$7.00 < \mathbf{7.50} < 8.00$	24	$-4.59^{+1.06}_{-5.00}$	$34.56^{+5.01}_{-0.59}$	$-2.20^{+1.40}_{-0.88}$
$8.00 < \mathbf{8.25} < 8.50$	118	$-6.53^{+\infty}_{-\infty}$	$35.69^{+\infty}_{-\infty}$	$-2.89^{+\infty}_{-\infty}$
$8.00 < \mathbf{8.25} < 8.50$ †	118	$-3.01^{+0.15}_{-0.20}$	$34.10^{+0.13}_{-0.11}$	$-1.26^{+0.30}_{-0.31}$
$8.50 < \mathbf{8.75} < 9.00$	364	$-2.62^{+0.07}_{-0.11}$	$34.22^{+0.11}_{-0.10}$	$-0.61^{+0.35}_{-0.31}$
$9.00 < \mathbf{9.25} < 9.50$	259	$-3.04^{+0.16}_{-0.22}$	$34.04^{+0.08}_{-0.07}$	$1.51^{+0.56}_{-0.51}$
$9.50 < \mathbf{9.75} < 10.00$	103	$-3.18^{+0.06}_{-0.10}$	$34.33^{+0.14}_{-0.12}$	$0.38^{+0.59}_{-0.52}$
$10.00 < \mathbf{10.25} < 10.50$	33	$-3.61^{+0.09}_{-0.21}$	$34.36^{+0.29}_{-0.22}$	$0.07^{+1.17}_{-0.90}$
$10.50 < \mathbf{10.75} < 11.00$	16	$-3.87^{+0.15}_{-0.49}$	$34.49^{+0.48}_{-0.32}$	$-0.12^{+1.81}_{-1.21}$
Redshift $z = 1.46$ Volume$= 23.06 \times 10^4$ Mpc^3				
		$\log \phi^*_{[OII]}$	$\log L^*_{[OII]}$ (Watts)	$\alpha_{[OII]}$
$8.00 < \mathbf{8.25} < 8.50$	154	$-13.28^{+\infty}_{-\infty}$	$37.73^{+\infty}_{-\infty}$	$-3.88^{+\infty}_{-\infty}$
$8.00 < \mathbf{8.25} < 8.50$ †	154	$-2.71^{+0.27}_{-0.43}$	$34.23^{+0.18}_{-0.14}$	$-2.09^{+0.46}_{-0.44}$
$8.50 < \mathbf{8.75} < 9.00$	457	$-2.22^{+0.05}_{-0.10}$	$34.14^{+0.11}_{-0.10}$	$-0.66^{+0.53}_{-0.47}$
$9.00 < \mathbf{9.25} < 9.50$	637	$-2.89^{+0.67}_{-0.04}$	$34.86^{+0.05}_{-0.92}$	$-1.43^{+4.62}_{-0.02}$
$9.50 < \mathbf{9.75} < 10.00$	386	$-2.68^{+0.05}_{-0.08}$	$34.44^{+0.08}_{-0.07}$	$0.56^{+0.39}_{-0.35}$
$10.00 < \mathbf{10.25} < 10.50$	287	$-2.99^{+0.14}_{-0.20}$	$34.80^{+0.14}_{-0.11}$	$-1.12^{+0.27}_{-0.26}$
$10.50 < \mathbf{10.75} < 11.00$	219	$-3.04^{+0.13}_{-0.18}$	$34.84^{+0.14}_{-0.12}$	$-0.97^{+0.31}_{-0.28}$
$11.00 < \mathbf{11.25} < 11.50$	46	$-4.17^{+0.58}_{-1.30}$	$34.35^{+0.19}_{-0.18}$	$2.41^{+2.11}_{-1.47}$

Table B1. Values of ρ_{SFR} in mass bins for the four redshift slices studied here. Values of ρ_{SFR} are presented first with 1 magnitude of extinction at Hα, then incorporating a treatment of extinction as a function of stellar mass, and finally our best estimates of ρ_{SFR} incorporating both dust and metallicity corrections (where appropriate) as a function of stellar mass.

Redshift $z = 0.63$ Volume= 8.09×10^4 Mpc^3

Log mass	1 mag Hα & Kennicutt 98		Extinction(mass) & Kewley et al. 04		Fully corrected	
(bin centre)	$\rho_{\text{SFR}_{\text{[OIII]}}}$ (M$_\odot$ yr^{-1} Mpc^{-3})		$\rho_{\text{SFR}_{\text{[OIII]}}}$ (M$_\odot$ yr^{-1} Mpc^{-3})		$\rho_{\text{SFR}_{\text{[OIII]}}}$ (M$_\odot$ yr^{-1} Mpc^{-3})	
	(>0.08)	(>1.00)	(>0.08)	(>1.00)	(>0.08)	(>1.00)
7.50	1.27E-03$^{+3.11E-05}_{-5.63E-05}$	1.06E-04$^{+6.22E-05}_{-6.56E-05}$	6.48E-04$^{+1.59E-05}_{-2.87E-05}$	5.41E-05$^{+3.17E-05}_{-0.00E+00}$	6.48E-04$^{+1.59E-05}_{-2.87E-05}$	5.41E-05$^{+3.17E-05}_{-0.00E+00}$
8.25	2.52E-03$^{+8.39E-05}_{-3.71E-04}$	7.66E-04$^{+1.33E-04}_{-3.80E-04}$	1.29E-03$^{+4.28E-05}_{-1.89E-04}$	3.91E-04$^{+6.78E-05}_{-1.94E-04}$	1.29E-03$^{+4.28E-05}_{-1.89E-04}$	3.91E-04$^{+6.78E-05}_{-1.89E-04}$
8.75	2.75E-03$^{+1.62E-04}_{-9.42E-04}$	1.97E-03$^{+1.76E-04}_{-9.43E-04}$	1.40E-03$^{+8.26E-05}_{-4.81E-04}$	1.01E-03$^{+8.96E-05}_{-4.81E-04}$	1.40E-03$^{+8.26E-05}_{-4.81E-04}$	1.01E-03$^{+8.96E-05}_{-4.81E-04}$
9.25	2.04E-03$^{+4.11E-04}_{-8.87E-04}$	1.82E-03$^{+3.63E-04}_{-8.77E-04}$	1.51E-03$^{+3.03E-04}_{-6.54E-04}$	1.34E-03$^{+2.67E-04}_{-6.46E-04}$	1.51E-03$^{+3.03E-04}_{-6.54E-04}$	1.34E-03$^{+2.67E-04}_{-6.46E-04}$
9.75	5.44E-04$^{+1.08E-04}_{-8.22E-05}$	6.53E-05$^{+3.93E-05}_{-4.02E-05}$	6.47E-04$^{+1.29E-04}_{-9.79E-05}$	7.77E-05$^{+4.68E-05}_{-4.78E-05}$	6.47E-04$^{+1.29E-04}_{-9.79E-05}$	7.77E-05$^{+4.68E-05}_{-4.78E-05}$

Redshift $z = 0.83$ Volume= 12.35×10^4 Mpc^3

Log mass	1 mag Hα & Kennicutt 98		Extinction(mass) & Kewley et al. 04		Fully corrected	
(bin centre)	$\rho_{\text{SFR}_{\text{[OIII]}}}$ (M$_\odot$ yr^{-1} Mpc^{-3})		$\rho_{\text{SFR}_{\text{[OIII]}}}$ (M$_\odot$ yr^{-1} Mpc^{-3})		$\rho_{\text{SFR}_{\text{[OIII]}}}$ (M$_\odot$ yr^{-1} Mpc^{-3})	
	(>0.12)	(>1.00)	(>0.12)	(>1.00)	(>0.12)	(>1.00)
7.50	8.71E-04$^{+1.11E-04}_{-4.17E-04}$	6.74E-05$^{+3.78E-05}_{-4.04E-05}$	4.40E-04$^{+3.39E-05}_{-2.53E-05}$	3.41E-05$^{+1.91E-05}_{-2.04E-05}$	4.40E-04$^{+3.39E-05}_{-2.53E-05}$	3.41E-05$^{+1.91E-05}_{-2.04E-05}$
8.25	1.90E-03$^{+1.39E-04}_{-9.08E-04}$	4.78E-04$^{+7.15E-05}_{-2.36E-04}$	9.60E-04$^{+3.18E-05}_{-1.19E-04}$	2.42E-04$^{+3.61E-05}_{-1.19E-04}$	9.60E-04$^{+3.18E-05}_{-1.19E-04}$	2.42E-04$^{+3.61E-05}_{-1.19E-04}$
8.75	3.33E-03$^{+2.21E-04}_{-1.59E-03}$	2.36E-03$^{+1.68E-04}_{-1.13E-03}$	1.68E-03$^{+8.63E-05}_{-5.70E-04}$	1.19E-03$^{+8.50E-05}_{-5.70E-04}$	1.68E-03$^{+8.63E-05}_{-5.70E-04}$	1.19E-03$^{+8.50E-05}_{-5.70E-04}$
9.25	2.00E-03$^{+2.23E-04}_{-9.58E-04}$	1.87E-03$^{+1.99E-04}_{-8.94E-04}$	1.46E-03$^{+1.55E-04}_{-6.54E-04}$	1.37E-03$^{+1.45E-04}_{-6.53E-04}$	1.46E-03$^{+1.55E-04}_{-6.54E-04}$	1.37E-03$^{+1.45E-04}_{-6.53E-04}$
9.75	1.68E-03$^{+7.14E-04}_{-8.55E-04}$	1.20E-03$^{+5.75E-04}_{-5.92E-04}$	1.98E-03$^{+8.08E-04}_{-7.57E-04}$	1.41E-03$^{+6.78E-04}_{-6.98E-04}$	1.98E-03$^{+8.08E-04}_{-7.57E-04}$	1.41E-03$^{+6.78E-04}_{-6.98E-04}$
10.25	6.68E-04$^{+3.72E-04}_{-3.37E-04}$	2.10E-04$^{+8.26E-05}_{-1.04E-04}$	1.31E-03$^{+5.53E-04}_{-2.91E-04}$	4.11E-04$^{+1.62E-04}_{-2.04E-04}$	1.31E-03$^{+5.53E-04}_{-2.91E-04}$	4.11E-04$^{+1.62E-04}_{-2.04E-04}$

Redshift $z = 1.19$ Volume= 19.06×10^4 Mpc^3

Log mass	1 mag Hα & Kennicutt 98		Extinction(mass) & Kewley et al. 04		Fully corrected: Extinction(mass) + Z	
(bin centre)	$\rho_{\text{SFR}_{\text{[OII]}}}$ (M$_\odot$ yr^{-1} Mpc^{-3})		$\rho_{\text{SFR}_{\text{[OII]}}}$ (M$_\odot$ yr^{-1} Mpc^{-3})		$\rho_{\text{SFR}_{\text{[OII]}}}$ (M$_\odot$ yr^{-1} Mpc^{-3})	
	(>0.55)	(>1.00)	(>0.55)	(>1.00)	(>0.55)	(>1.00)
7.50	4.65E-04$^{+1.33E-04}_{-2.28E-04}$	3.03E-04$^{+7.94E-05}_{-1.47E-04}$	1.90E-04$^{+5.43E-05}_{-9.32E-05}$	1.24E-04$^{+3.25E-05}_{-6.02E-05}$	1.21E-03$^{+6.52E-05}_{-1.12E-04}$	7.91E-04$^{+3.90E-05}_{-7.23E-05}$
8.25	2.07E-03$^{+2.18E-04}_{-9.87E-04}$	1.49E-03$^{+1.59E-04}_{-7.11E-04}$	8.45E-04$^{+8.90E-05}_{-4.04E-04}$	6.08E-04$^{+6.49E-05}_{-2.90E-04}$	1.77E-03$^{+1.07E-04}_{-4.84E-04}$	1.27E-03$^{+7.80E-05}_{-3.49E-04}$
8.75	7.42E-03$^{+4.44E-04}_{-3.55E-03}$	6.59E-03$^{+3.71E-04}_{-3.15E-03}$	3.03E-03$^{+1.82E-04}_{-1.45E-03}$	2.69E-03$^{+1.52E-04}_{-1.29E-03}$	3.95E-03$^{+2.18E-04}_{-1.74E-03}$	3.51E-03$^{+1.82E-04}_{-1.54E-03}$
9.25	7.75E-03$^{+5.35E-04}_{-3.70E-03}$	7.67E-03$^{+5.20E-04}_{-3.66E-03}$	3.17E-03$^{+2.19E-04}_{-1.51E-03}$	3.13E-03$^{+2.12E-04}_{-1.50E-03}$	3.29E-03$^{+2.62E-04}_{-1.81E-03}$	3.26E-03$^{+2.55E-04}_{-1.80E-03}$
9.75	3.84E-03$^{+4.80E-04}_{-1.84E-03}$	3.78E-03$^{+4.63E-04}_{-1.81E-03}$	2.61E-03$^{+3.25E-04}_{-1.25E-03}$	2.57E-03$^{+3.14E-04}_{-1.23E-03}$	2.66E-03$^{+3.90E-04}_{-1.50E-03}$	2.62E-03$^{+3.77E-04}_{-1.47E-03}$
10.25	1.31E-03$^{+2.96E-04}_{-6.27E-04}$	1.27E-03$^{+2.85E-04}_{-6.10E-04}$	1.72E-03$^{+3.90E-04}_{-8.25E-04}$	1.68E-03$^{+3.75E-04}_{-8.03E-04}$	1.92E-03$^{+4.68E-04}_{-9.91E-04}$	1.87E-03$^{+4.50E-04}_{-9.64E-04}$
10.75	9.11E-04$^{+3.35E-04}_{-4.42E-04}$	8.92E-04$^{+3.08E-04}_{-4.31E-04}$	2.41E-03$^{+8.89E-04}_{-1.17E-03}$	2.37E-03$^{+8.18E-04}_{-1.14E-03}$	3.05E-03$^{+1.07E-03}_{-1.41E-03}$	2.99E-03$^{+9.82E-04}_{-1.37E-03}$

Redshift $z = 1.46$ Volume= 23.06×10^4 Mpc^3

Log mass	1 mag Hα & Kennicutt 98		Extinction(mass) & Kewley et al. 04		Fully corrected: Extinction(mass) + Z	
(bin centre)	$\rho_{\text{SFR}_{\text{[OII]}}}$ (M$_\odot$ yr^{-1} Mpc^{-3})		$\rho_{\text{SFR}_{\text{[OII]}}}$ (M$_\odot$ yr^{-1} Mpc^{-3})		$\rho_{\text{SFR}_{\text{[OII]}}}$ (M$_\odot$ yr^{-1} Mpc^{-3})	
	(>1.42)	(>1.00)	(>1.42)	(>1.00)	(>1.42)	(>1.00)
8.25	3.61E-03$^{+3.18E-04}_{-1.72E-03}$	5.37E-03$^{+5.42E-04}_{-2.58E-03}$	1.47E-03$^{+1.30E-04}_{-7.03E-04}$	2.19E-03$^{+2.21E-04}_{-1.05E-03}$	3.68E-03$^{+1.56E-04}_{-8.44E-04}$	5.48E-03$^{+2.65E-04}_{-1.26E-03}$
8.75	1.11E-02$^{+5.54E-04}_{-5.30E-03}$	1.30E-02$^{+7.91E-04}_{-6.24E-03}$	4.53E-03$^{+2.26E-04}_{-2.16E-03}$	5.32E-03$^{+3.23E-04}_{-2.55E-03}$	6.57E-03$^{+2.71E-04}_{-2.60E-03}$	7.71E-03$^{+3.88E-04}_{-3.06E-03}$
9.25	2.25E-02$^{+1.62E-03}_{-1.09E-02}$	2.45E-02$^{+1.46E-03}_{-1.23E-02}$	9.17E-03$^{+6.59E-04}_{-4.45E-03}$	1.00E-02$^{+5.96E-04}_{-5.03E-03}$	9.92E-03$^{+7.91E-04}_{-5.34E-03}$	1.08E-02$^{+7.16E-04}_{-6.04E-03}$
9.75	1.86E-02$^{+1.11E-03}_{-8.90E-04}$	1.88E-02$^{+1.15E-03}_{-9.03E-04}$	1.26E-02$^{+7.54E-04}_{-6.03E-04}$	1.27E-02$^{+7.80E-04}_{-6.08E-04}$	1.28E-02$^{+9.06E-04}_{-7.23E-04}$	1.29E-02$^{+9.37E-04}_{-7.30E-04}$
10.25	1.33E-02$^{+8.99E-04}_{-6.34E-03}$	1.41E-02$^{+1.02E-03}_{-6.73E-03}$	1.75E-02$^{+1.18E-03}_{-8.34E-03}$	1.85E-02$^{+1.33E-03}_{-8.84E-03}$	1.89E-02$^{+1.42E-03}_{-1.00E-02}$	2.01E-02$^{+1.60E-03}_{-1.06E-02}$
10.75	1.28E-02$^{+1.01E-03}_{-6.13E-03}$	1.34E-02$^{+1.11E-03}_{-6.39E-03}$	3.40E-02$^{+2.68E-03}_{-1.62E-02}$	3.54E-02$^{+2.94E-03}_{-1.69E-02}$	4.17E-02$^{+3.22E-03}_{-1.95E-02}$	4.34E-02$^{+3.53E-03}_{-2.03E-02}$
11.25	3.64E-03$^{+6.51E-04}_{-1.74E-03}$	3.64E-03$^{+6.54E-04}_{-1.74E-03}$	1.78E-02$^{+3.19E-03}_{-8.52E-03}$	1.78E-02$^{+3.21E-03}_{-8.53E-03}$	2.44E-02$^{+3.84E-03}_{-1.02E-02}$	2.44E-02$^{+3.85E-03}_{-1.02E-02}$